Dissipative particle dynamics modeling of red blood cells

6

D. A. Fedosov[#], B. Caswell[†], G. E. Karniadakis[#]

Division of Applied Mathematics[#]
Division of Engineering[†]
Brown University
Providence

Capsules and red blood cells suspended in various flows exhibit a rich dynamics due to the deformability of the enclosing membranes. To accurately capture statics and dynamics, mechanical models of the membrane must be available incorporating shear elasticity, bending rigidity, and membrane viscosity. In the approach described in this chapter, the membrane of a red blood cell is modeled as a network of interconnected nonlinear springs emulating the membrane spectrin network. Dissipative forces in the network mimic the effect of the lipid bilayer. The macroscopic elastic properties of the network are analytically related to the spring parameters to circumvent ad-hoc adjustment. Chosen parameters values yield model membranes that reproduce optical tweezer stretching experiments. When probed with an attached oscillating microbead, predicted viscoelastic properties are in good agreement with experiments using magnetic optical twisting cytometry. In shear flow, red blood cells respond by tumbling at low shear rates and tank-treading at high shear rates. In transitioning between these regimes, the membrane exhibits substantial deformation controlled largely by flexural stiffness. Raising the membrane or internal fluid viscosity shift the transition threshold to higher shear rates and reduces the tank-treading frequency. Simulations reveal that a purely elastic membrane model devoid of a viscous properties cannot adequately capture the cell dynamics. Results are presented to demonstrate the dependence of transition thresholds from biconcave to parachute shapes in capillary flow on the cell properties and the mean flow velocity.

6.1 Introduction

Red blood cells are soft biconcave capsules with an average diameter 7.8 μm and an interior viscous liquid enclosed by a viscoelastic membrane. The cell membrane consists of a nearly incompressible lipid bilayer attached to a spectrin protein network held together by short actin filaments known as the cytoskeleton. This membrane structure ensures the integrity of the cell in narrow capillaries whose cross-section is smaller than the size of the biconcave disk (e.g., Fung 1993). Consistent with the spectrin cytoskeleton structure, the membrane can be modeled as a network of viscoelastic springs mediating elastic and viscous response. Flexural stiffness can be introduced as a network bending energy, and constraints on the surface area and volume can be imposed to enforce the area incompressibility of the lipid bilayer and the volume incompressibility of the interior fluid.

A number of theoretical and numerical analyses have sought to describe cell behavior and deformation in a variety of flows. Examples include models of ellipsoidal cells enclosed by viscoelastic membranes (e.g., Abkarian *et al.* 2007, Skotheim & Secomb 2007), numerical models based on shell theory, (e.g., Fung 1993, Eggleton & Popel 1998, Pozrikidis 2005), and discrete descriptions at the spectrin protein level (e.g., Discher *et al.* 1998, Li *et al.* 2005) or at a mesoscopic level (e.g., Noguchi & Gompper 2005, Dupin *et al.* 2007, Pivkin & Karniadakis 2008). The membranes of healthy red blood cells exhibit nonlinear elastic response in steady stretching and viscous response in dynamic testing. Most existing membrane models incorporate only the elastic response. Fluid-and solid-like models demand high computational costs due to the strong coupling of solid mechanics and fluid flow.

Semicontinuum models of deformable cells employ boundary-element, immersed-boundary, and front-tracking methods to combine a discrete membrane representation with the interior and exterior flow (e.g., Eggleton & Popel 1998, Pozrikidis 2005). A membrane is described by a set of point particles whose motion is coupled to a flow computed on an Eulerian grid. Most models assume that the fluid viscosities are equal and ignore thermal fluctuations (e.g., Noguchi & Gompper 2005). Modeling a cell at the spectrin-protein level is constrained by high computational cost.

Mesoscopic modeling of viscoelastic capsules and red blood cells are currently being developed to describe three-dimensional motion (e.g., Noguchi & Gompper 2005, Dupin *et al.* 2007, Pivkin & Karniadakis 2008). Noguchi & Gompper (2005) simulated the deformation of vesicles enclosed by viscoelastic membranes using the method of multi-particle collision dynamics (e.g., Malevanets & Kapral 1999). Dupin *et al.* (2007) combined a lattice-Boltzmann method (e.g., Succi 2001) with a discrete membrane representation neglect-

ing the membrane viscosity and the occurrence of thermal fluctuations. The implementation smears the sharp interface between the external and internal fluid requited by the impenetrability of the membrane.

The elasticity of the red blood cell membrane is attributed to a spectrin network of approximately 27×10^3 nodes. The population number was reduced (coarse-grained) by Pivkin & Karniadakis (2008) by employing a dissipative particle dynamics (DPD) approach to represent cell membranes with networks of only 500 DPD particles connected with springs. (e.g., Hoogerbrugge & Koelman 1992) Their model is the starting point for the work discussed in this chapter.

First, a theoretical analysis will be presented for a membrane network model exhibiting specified macroscopic membrane properties without parameter adjustment. The predicted cell mechanical properties will be compared with optical tweezers stretching experiments by Suresh *et al.* (2005), and the predicted rheological properties will be compared with magnetic optical twisting cytometry experiments by Puig-de-Morales-Marinkovic *et al.* (2007). Red blood dynamics in shear flow showing tumbling and tank-treading will be studied in detail with a view to delineating the effect of the membrane shear moduli, bending rigidity, external, internal, and membrane viscosities. Simulations of cell motion in Poiseuille flow will confirm that the biconcave-to-parachute transition depend on the flow strength and membrane properties. Comparison with available experiments will demonstrate that the computational model is able to accurately describe realistic red blood cell motion.

Comparison of the numerical simulations with theoretical predictions by Abkarian *et al.* (2007), Skotheim & Secomb (2007), and others will reveal discrepancies suggesting that the current theoretical models are only qualitatively accurate due to strong simplifications.

6.2 Mathematical framework

In the theoretical model, the membrane of a red blood cell is represented by a viscoelastic network. The motion of the internal and external fluids is described by the method of dissipative particle dynamics (DPD) (e.g., Hoogerbrugge & Koelman 1992). The membrane model is sufficiently general to be used with other simulation techniques, such as Brownian dynamics, lattice Boltzmann, multiparticle collision dynamics, and the immerse-boundary method.

6.2.1 Dissipative particle dynamics

Dissipative particle dynamics (DPD) is a mesoscopic simulation technique for computing the flow of complex fluids. A DPD system of N particles represents lumps of atoms or molecules described by the particle position, $\mathbf{r}_i$, velocity, $\mathbf{v}_i$, and mass m_i, where $i = 1, \ldots, N$. Particle interactions are mediated by conservative (C), dissipative (D), and random (R) interparticle forces given by

$$\mathbf{F}_{ij}^C = F_{ij}^C(r_{ij})\,\hat{\mathbf{r}}_{ij}, \qquad \mathbf{F}_{ij}^D = -\gamma\,\omega^D(r_{ij})\,(\mathbf{v}_{ij}\cdot\hat{\mathbf{r}}_{ij})\hat{\mathbf{r}}_{ij},$$

$$\mathbf{F}_{ij}^R = \sigma\,\omega^R(r_{ij})\,\frac{\xi_{ij}}{\sqrt{dt}}\hat{\mathbf{r}}_{ij}, \tag{6.2.1}$$

where $\mathbf{r}_{ij}$ is the distance between the ith and jth particle, $\hat{\mathbf{r}}_{ij} = \mathbf{r}_{ij}/r_{ij}$ is a unit vector, $r_{ij} = |\mathbf{r}_{ij}|$, and $\mathbf{v}_{ij} = \mathbf{v}_i - \mathbf{v}_j$. The coefficients γ and σ are the amplitudes of the dissipative and random forces, and the factors ω^D and ω^R are weights. The random force definition employs normally distributed random variables ξ_{ij} with zero mean, unit variance, and pairwise symmetry, $\xi_{ij} = \xi_{ji}$. The forces vanish beyond a cutoff radius, r_c, which defines the DPD length scale.

A typical conservative force is

$$F_{ij}^C(r_{ij}) = \begin{cases} a_{ij}(1 - r_{ij}/r_c) & \text{for } r_{ij} \le r_c, \\ 0 & \text{for } r_{ij} > r_c, \end{cases} \tag{6.2.2}$$

where a_i and a_j are conservative force coefficients for the ith and jth particle. The random force weight function $\omega^R(r_{ij})$ is chosen to be

$$\omega^R(r_{ij}) = \begin{cases} (1 - r_{ij}/r_c)^m & \text{for } r_{ij} \le r_c, \\ 0 & \text{for } r_{ij} > r_c. \end{cases} \tag{6.2.3}$$

In the original DPD method, m was set to unity. Different exponent values can be used to alter the fluid viscosity and increase the Schmidt number $\mathrm{Sc} = \nu/D$, where D is the self-diffusion,and $\nu = \mu/\rho$ is the kinematic viscosity (e.g., Fan *et al.* 2006, 2008).

Temperature control is achieved by balancing random and dissipative forces according to the fluctuation-dissipation theorem,

$$\omega^D(r_{ij}) = \left[\omega^R(r_{ij})\right]^2, \qquad \sigma^2 = 2\gamma k_B T, \tag{6.2.4}$$

where T is the equilibrium temperature and k_B is the Boltzmann constant (e.g., Espanol & Warren 1995).

The particles move in space according to the Newton's second law of motion,

$$\frac{\mathrm{d}\mathbf{r}_i}{\mathrm{d}t} = \mathbf{v}_i, \qquad \frac{\mathrm{d}\mathbf{v}_i}{\mathrm{d}t} = \frac{1}{m_i}\sum_{j\neq i}\mathbf{F}_{ij}, \tag{6.2.5}$$

where $\mathbf{r}_i$ is the particle position and $\mathbf{F}_{ij}$ is the force exerted on the ith by the jth particle. The particle equation of motion is integrated with the velocity Verlet algorithm (e.g., Allen & Tildesley 1987).

6.2.2 Mesoscopic viscoelastic membrane model

The cell membrane is represented by a two-dimensional curved triangulated network defined by N_v vertices, $\mathbf{x}_i$, connected by N_s springs (edges) to form N_t triangular faces, where $i = 1, \ldots, N_v$. The total energy of the network consists of an in-plane elastic energy, a viscous dissipation energy (IP), a bending energy (B), a surface area energy (A), and a volume energy (V),

$$V(\{\mathbf{x}_i\}) = V_{IP} + V_B + V_A + V_V. \tag{6.2.6}$$

The individual energy components are discussed in this section.

Elastic energy and viscous dissipation

The in-plane elastic energy is given by

$$V_{IP} = \sum_{j=1,\ldots,N_s}[U_{IPS}(\ell_j) + U_{IPV}(\Delta v_j)] + \sum_{k=1}^{N_t}\frac{C_q}{A_k^q}, \tag{6.2.7}$$

where IPS stands for the in-plane spring energy and IPV stands for the in-plane viscous dissipation. The first sum in (6.2.7) expresses the contribution of viscoelastic springs; ℓ_j is the length of the jth spring and Δv_j is the relative velocity of the spring end points. The second sum expresses a stored elastic energy assigned to each triangular patch; A_k is the area of the kth triangle. The constant C_q and exponent q will be defined.

We employ the worm-like chain (WLC) model alone or in combination with a stored elastic energy (WLC-C) or a power function (POW) potential (WLC-POW). The WLC energy is given by

$$U_{WLC} = \frac{k_B T \ell_m}{4p}\frac{3x^2 - 2x^3}{1-x}. \tag{6.2.8}$$

where $x = \ell/\ell_m \in (0,1)$, ℓ_m is the maximum spring extension, and p is the persistence length. The power-function energy is given by

$$U_{POW} = \frac{k_p}{(n-1)\ell^{n-1}}, \tag{6.2.9}$$

where k_p is a spring constant and n is a specified exponent.

Attractive forces exerted by WLC springs cause element compression. The second term in the WLC-C model (6.2.7) contributes an elastic energy that tends to expand the area. The equilibrium state of a single triangular plaquette with WLC-C energy defines an equilibrium spring length, ℓ_0. A relationship between the WLC spring parameters and C_q can be obtained by setting the Cauchy stress derived from the virial theorem to zero (e.g., Allen & Tildesley 1987),

$$C_q^{WLC} = \frac{\sqrt{3}A_0^{q+1}}{4pq\ell_m}\, k_B T\, \frac{4x_0^2 - 9x_0 + 6}{1 - x_0}, \tag{6.2.10}$$

where $x_0 = \ell_0/\ell_m$ and $A_0 = \sqrt{3}l_0^2/4$ (e.g., Dao *et al.* 2006). Given the equilibrium length and spring parameters, this formula provides with a value for C_q in (6.2.7) for a chosen q.

Similar considerations apply to the WLC-POW model where a finite spring length can be defined by balancing the WLC and POW forces. In this manner, p and k_p can be related to the WLC parameters and a chosen exponent, n. Since the POW term is able to mediate WLC area compression, the stored elastic energy is omitted and C_q is set to zero. The viscous component associated with each spring will be defined.

Bending energy

The bending energy is concentrated at the element edges according to the bending potential

$$V_B = \sum_{j=1}^{N_s} k_b \left[1 - \cos(\theta_j - \theta_0)\right], \tag{6.2.11}$$

where k_b is a bending modulus, θ_j is the instantaneous angle formed between two adjacent triangles sharing the jth edge, and θ_0 is the spontaneous angle. A schematic illustration of these angles is shown in figure 6.2.1.

Area and volume constraints

The last two terms in (6.2.6) enforce area conservation of the lipid bilayer and incompressibility of the interior fluid as area and volume constraints,

$$V_A = \frac{k_a}{2A_0^{tot}}\,(A - A_0^{tot})^2 + \frac{k_d}{2A_0}\sum_{j=1}^{N_t}(A_j - A_0)^2, \tag{6.2.12}$$

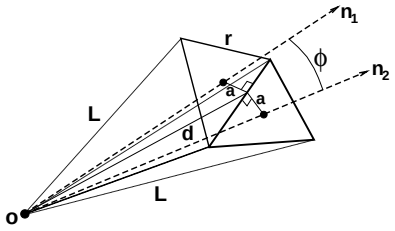

Figure 6.2.1 Illustration of two equilateral triangles on the surface of a sphere of radius L.

and

$$V_V = \frac{k_v^2}{2V_0^{tot}}\,(V - V_0^{tot})^2, \tag{6.2.13}$$

where k_a, k_d and k_v are constraint constants for global area, local area, and volume constraints, A and V are the instantaneous membrane area and cell volume, and A_0^{tot} and V_0^{tot} are their respective specified values.

Nodal forces

Nodal forces $\mathbf{f}_i$ are derived from the elastic network energy by taking partial derivatives,

$$\mathbf{f}_i = -\frac{\partial V(\{\mathbf{x}_i\})}{\partial \mathbf{x}_i}, \tag{6.2.14}$$

for $i = 1, \ldots, N_v$. Exact expressions are outlined in the appendix.

6.2.3 Triangulation

According to Evans & Skalak (1980), the average shape of a normal red blood cell is described by

$$z = \pm D_0 \left(1 - \frac{4(x^2+y^2)}{D_0^2}\right)^{1/2} \left(a_0 + a_1\frac{x^2+y^2}{D_0^2} + a_2\frac{(x^2+y^2)^2}{D_0^4}\right), \tag{6.2.15}$$

where $D_0 = 7.82$ μm is the cell diameter, $a_0 = 0.0518$, $a_1 = 2.0026$, and $a_2 = -4.491$. The cell area and volume are, respectively, 135 μm^2 and 94 μm^3.

In the simulations, the membrane network structure is generated by triangulating the unstressed equilibrium shape described by (6.2.15). The cell

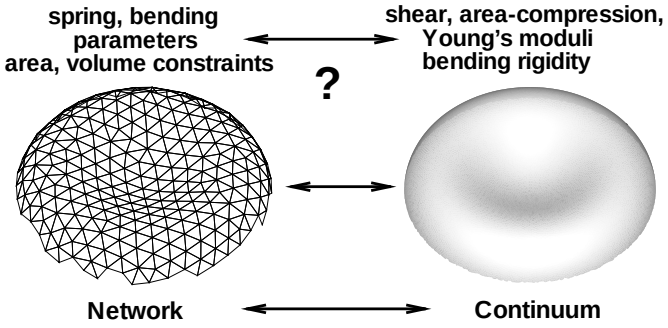

Figure 6.3.1 Illustration of a membrane network and corresponding continuum model.

shape is first imported into a commercial grid generation software to produce an initial triangulation based on the advancing-front method. Subsequently, free-energy relaxation is performed by flipping the diagonals of quadrilateral elements formed by two adjacent triangles, while the vertices are constrained to move on the prescribed surface. The relaxation procedure includes only elastic in-plane and bending energy components.

6.3 Membrane mechanical properties

Several parameters must be chosen in the membrane network model to ensure a desired mechanical response. Figure 6.3.1 depicts a network model and its continuum counterpart. To circumvent ad-hoc parameter adjustment, we derive relationships between local model parameters and network macroscopic properties for an elastic hexagonal network. A similar analysis for a two-dimensional particulate sheet of equilateral triangles was presented by Dao *et al.* (2006).

Figure 6.3.2 illustrates an element in a hexagonal network with vertex $\mathbf{v}$ placed at the origin of a local Cartesian system. Using the virial theorem, we find that the Cauchy stress tensor at $\mathbf{v}$ is

$$\tau_{\alpha\beta}=-\frac{1}{S}\left[\frac{f(r_1)}{r_1}r_1^\alpha r_1^\beta+\frac{f(r_2)}{r_2}r_2^\alpha r_2^\beta+\frac{f(|\mathbf{r}_2-\mathbf{r}_1|)}{|\mathbf{r}_2-\mathbf{r}_1|}(r_2^\alpha-r_1^\alpha)(r_2^\beta-r_1^\beta)\right]$$
$$-\Big(q\frac{C_q}{A^{q+1}}+\frac{k_a(A_0^{tot}-N_tA)}{A_0^{tot}}+\frac{k_d(A_0-A)}{A_0}\Big)\delta_{\alpha\beta}, \qquad (6.3.1)$$

where α and β stand for x or y, $f(r)$ is the spring force, N_t is the total number

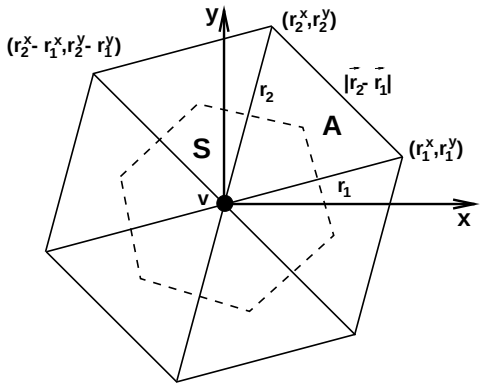

Figure 6.3.2 Illustration of an element in a hexagonal triangulation.

of triangles, $A_0^{tot} = N_t A_0$, $S = 2A_0$, $\delta_{\alpha\beta}$ is the Kronecker delta, and S is the area of the hexagonal element centered at $\mathbf{v}$. (e.g., Allen & Tildesley 1987).

6.3.1 Shear modulus

The shear modulus is derived from the network deformation by applying to a material vector embedded in the surface, $\mathbf{r}_1$, an engineering shear strain γ, so that the deformed material vector is

$$\mathbf{r}_1' = \mathbf{r}_1 \cdot \mathbf{J} = \begin{bmatrix} r_1^x + \frac{1}{2} r_1^y \\ \frac{1}{2} r_1^x \gamma + r_1^y \end{bmatrix}, \tag{6.3.2}$$

where

$$\mathbf{J} = \begin{bmatrix} 1 & \gamma/2 \\ \gamma/2 & 1 \end{bmatrix} + O(\gamma^2) \tag{6.3.3}$$

is the linear strain tensor and $\mathbf{r}_1 = (r_1^x; r_1^y)$, as shown in figure 6.3.2. Because the shear deformation is area preserving, only spring forces contribute to the membrane shear modulus.

Expanding τ_{xy} in a Taylor series, we find that

$$\tau_{xy}' = \tau_{xy} + \left.\frac{\partial \tau_{xy}'}{\partial \gamma}\right|_{\gamma=0} \gamma + O(\gamma^2). \tag{6.3.4}$$

The linear shear modulus of the network is

$$\mu_0 = \left.\frac{\partial \tau_{xy}'}{\partial \gamma}\right|_{\gamma=0}. \tag{6.3.5}$$

For example, differentiating the first term of τ_{xy} yields

$$\frac{\partial}{\partial\gamma}\Big(\frac{f(r_1')}{r_1'}r_1^{x'}r_1^{y'}\Big)_{\gamma=0}=\Big(\frac{\partial\frac{f(r_1)}{r_1}}{\partial r_1}\frac{(r_1^x r_1^y)^2}{r_1}+\frac{f(r_1)r_1}{2}\Big)_{r_1=\ell_0}. \tag{6.3.6}$$

Using the vector-product definition of the area of a triangle, we obtain

$$(r_1^x r_1^y)^2+(r_2^x r_2^y)^2+(r_2^x-r_1^x)^2(r_2^y-r_1^y)^2=2A_0^2. \tag{6.3.7}$$

The linear shear modulus of the WLC-C and WLC-POW models is

$$\mu_0^{WLC-C}=\frac{\sqrt{3}k_BT}{4p\ell_m x_0}\Big(\frac{3}{4(1-x_0)^2}-\frac{3}{4}+4x_0+\frac{x_0}{2(1-x_0)^3}\Big) \tag{6.3.8}$$

and

$$\mu_0^{WLC-POW}=\frac{\sqrt{3}k_BT}{4p\ell_m x_0}\Big(\frac{x_0}{2(1-x_0)^3}-\frac{1}{4(1-x_0)^2}+\frac{1}{4}\Big)+\frac{\sqrt{3}k_p(m+1)}{4\ell_0^{m+1}}. \tag{6.3.9}$$

6.3.2 Compression modulus

The linear elastic area compression modulus K is found from the in-plane pressure following a small area expansion as

$$p=-\frac{1}{2}(\tau_{xx}+\tau_{yy})=\frac{3\,\ell}{4A}f(\ell)+q\frac{C_q}{A^{q+1}}+\frac{(k_a+k_d)(A_0-A)}{A_0}. \tag{6.3.10}$$

Defining the compression modulus as

$$K=-\frac{\partial p}{\partial\log A}\Big|_{A=A_0}=-\frac{1}{2}\frac{\partial p}{\partial\log\ell}\Big|_{\ell=\ell_0}=-\frac{1}{2}\frac{\partial p}{\partial\log x}\Big|_{x=x_0}, \tag{6.3.11}$$

and using equations (6.3.10) and (6.3.11), we obtain

$$K^{WLC-C}=\frac{\sqrt{3}k_BT}{4p\ell_m(1-x_0)^2}\Big[\Big(q+\frac{1}{2}\Big)\,(4x_0^2-9x_0+6)+\frac{1+2(1-x_0)^3}{1-x_0}\Big]+k_a+k_d \tag{6.3.12}$$

and

$$K^{WLC-POW}=2\mu_0^{WLC-POW}+k_a+k_d. \tag{6.3.13}$$

For $q=1$, we find

$$K^{WLC-C}=2\mu_0^{WLC-C}+k_a+k_d. \tag{6.3.14}$$

For the nearly constant-area membrane enclosing a red blood cell, the compression modulus is much larger than the shear elastic modulus.

The Young modulus and Poisson's ratio of the two-dimensional sheet are given by

$$Y = 4\,\frac{K\mu_0}{K+\mu_0}, \qquad \nu = \frac{K-\mu_0}{K+\mu_0}. \tag{6.3.15}$$

As $K \to \infty$, we obtain $Y \to 4\mu_0$ and $\nu \to 1$, as required. To ensure a nearly constant area, we set $k_a + k_d \gg \mu_0$. In practice, the values $\mu_0 = 100$ and $k_a + k_d = 5000$, yield a nearly incompressible membrane with Young's modulus about 2% smaller than the asymptotic value $4\mu_0$.

The analytical expressions given in (6.3.15) were verified by numerical tests on a regular two-dimensional sheet of springs. The two-dimensional sheet was confirmed to be isotropic for small shear strains and stretches, but was found to be anisotropic for large deformations (e.g., Fedosov 2010).

6.3.3 Bending rigidity

Helfrich (1973) proposed an expression for the bending energy of the membrane of a red blood cell,

$$E_c = \frac{k_c}{2} \iint (C_1 + C_2 - 2C_0)^2 \,\mathrm{d}A + k_g \iint C_1 C_2 \,\mathrm{d}A, \tag{6.3.16}$$

where C_1 and C_2 are the principal curvatures, C_0 is the spontaneous curvature, and k_c, k_g are bending rigidities. The second term on the right-hand side of(6.3.16) is constant and thus inconsequential for any closed surface.

A relationship between the bending modulus, k_b, and the macroscopic membrane bending rigidity, k_c, can be derived for a spherical shell. Figure 6.2.1 shows two equilateral triangles with edge length r whose vertices lie on a sphere of radius L. The angle between the triangle normals $\mathbf{n}_1$ and $\mathbf{n}_2$ is denoted by ϕ. In the case of a spherical shell, the total energy in (6.3.16) is found to be

$$E_c = 8\pi k_c\Big(1 - \frac{C_0}{C_1}\Big)^2 + 4\pi k_g = 8\pi k_c\Big(1 - \frac{L}{L_0}\Big)^2 + 4\pi k_g, \tag{6.3.17}$$

where $C_1 = C_2 = 1/L$ and $C_0 = 1/L_0$. In the network model, the energy of the triangulated sphere is

$$V_B = N_s\, k_b\, [1 - \cos(\phi - \phi_0)]. \tag{6.3.18}$$

Expanding $\cos(\phi - \phi_0)$ in a Taylor series around $\phi - \phi_0$ provides us with the leading term

$$V_B = \frac{1}{2}\, N_s k_b (\phi - \phi_0)^2 + O\big((\phi - \phi_0)^4\big). \tag{6.3.19}$$

With reference to figure 6.3.2, we find that $2a \approx \phi L$ or $\phi = r/(\sqrt{3}L)$, and $\phi_0 = r/(\sqrt{3}L_0)$.

For a sphere, $A = 4\pi L^2 \approx N_t A_0 = \sqrt{3}N_t r^2/4 = \sqrt{3}N_s r^2/6$, and $r^2/L^2 = 8\pi\sqrt{3}/N_s$. Finally, we obtain

$$V_B = \frac{1}{2} N_s k_b \left(\frac{r}{\sqrt{3}L} - \frac{r}{\sqrt{3}L_0}\right)^2 = \frac{N_s k_b r^2}{6L^2}\left(1 - \frac{L}{L_0}\right)^2 = \frac{4\pi k_b}{\sqrt{3}}\left(1 - \frac{L}{L_0}\right)^2. \quad (6.3.20)$$

Equating the macroscopic bending energy E_c to V_B for $k_g = -4k_c/3$ and $C_0 = 0$, we obtain $k_b = 2k_c/\sqrt{3}$ in agreement with the limit of a continuum approximation (e.g., Lidmar *et al.* 2003).

The spontaneous angle ϕ_0 is set according to the total number of vertices on the sphere, N_v. It can be shown that $\cos\phi = 1 - 1/[6(L^2/r^2 - 1/4)]$ and the number of side is $N_s = 2N_v - 4$. The bending stiffness, k_b, and spontaneous angle, ϕ_0, are given by

$$k_b = \frac{2}{\sqrt{3}} k_c, \qquad \phi_0 = \arccos\left(\frac{\sqrt{3}(N_v - 2) - 5\pi}{\sqrt{3}(N_v - 2) - 3\pi}\right). \quad (6.3.21)$$

6.3.4 Membrane viscosity

Since interparticle dissipative interaction is an intrinsic part of the formulation, incorporating dissipative and random forces into springs fits naturally into the DPD scheme. Straightforward implementation of standard DPD dissipative and random interactions expressed by (6.2.1) is insufficient. The reason is that, when projected onto the connecting vector, the contribution of the inter-particle relative velocity, $\mathbf{v}_{ij}$, is negligible for small dissipative coefficients γ. Large values promote numerical instability.

Best performance is achieved by assigning to each spring a viscous dissipation force $-\gamma \mathbf{v}_{ij}$, where γ is a scalar coefficient. However, any alteration of the dissipative forces requires a corresponding change in fluctuating forces consistent with the fluctuation-dissipation balance to ensure a constant membrane temperature, $k_B T$. The general framework of the fluid-particle model is employed with the following definitions

$$\mathbf{F}^D_{ij} = -\mathbf{T}_{ij} \cdot \mathbf{v}_{ij}, \qquad \mathbf{T}_{ij} = A(r_{ij})\,\mathbf{I} + B(r_{ij})\,\mathbf{e}_{ij}\mathbf{e}_{ij}, \quad (6.3.22)$$

and

$$\mathbf{F}^R_{ij}\,\mathrm{d}t = \sqrt{2k_B T}\left(\tilde{A}(r_{ij})\,\mathrm{d}\overline{\mathbf{W}^S_{ij}} + \tilde{B}(r_{ij})\frac{1}{3}\,\mathrm{tr}[\mathrm{d}\mathbf{W}_{ij}]\,\mathbf{I} + \tilde{C}(r_{ij})\,\mathrm{d}\mathbf{W}^A_{ij}\right) \cdot \mathbf{e}_{ij}, \quad (6.3.23)$$

where superscripts R and D stand for "random" and "dissipative", $\mathbf{I}$ is the identity matrix, $\mathrm{tr}[\mathrm{d}\mathbf{W}_{ij}]$ is the trace of a random matrix of independent Wiener increments $\mathrm{d}\mathbf{W}_{ij}$ whose symmetric and anti-symmetric parts are denoted with superscripts S and A, and

$$\mathrm{d}\overline{\mathbf{W}_{ij}^{S}} \equiv \mathrm{d}\mathbf{W}_{ij}^{S} - \frac{1}{3}\mathrm{tr}[d\mathbf{W}_{ij}^{S}]\,\mathbf{I} \tag{6.3.24}$$

is the traceless symmetric part (e.g., Espanol 1998) . The scalar weight functions $A(r)$, $B(r)$, $\tilde{A}(r)$, $\tilde{B}(r)$, and $\tilde{C}(r)$ are related by

$$\begin{aligned} A(r) &= \frac{1}{2}\left[\tilde{A}^2(r)+\tilde{C}^2(r)\right], \\ B(r) &= \frac{1}{2}\left[\tilde{A}^2(r)-\tilde{C}^2(r)\right]+\frac{1}{3}\left[\tilde{B}^2(r)-\tilde{A}^2(r)\right]. \end{aligned} \tag{6.3.25}$$

The standard forms of the dissipative and random forces are recovered by setting $\tilde{A}(r) = \tilde{C}(r) = 0$ and $B(r) = \gamma$. We employ spatially constant weight functions $A(r) = \gamma^T$, $B(r) = \gamma^C$, and $\tilde{C}(r) = 0$. where γ^T and γ^C are dissipative coefficients. Accordingly,

$$\mathbf{T}_{ij} = \gamma^T\mathbf{I} + \gamma^C\mathbf{e}_{ij}\mathbf{e}_{ij} \tag{6.3.26}$$

and the dissipative interaction force becomes

$$\mathbf{F}_{ij}^{D} = -\left(\gamma^T\mathbf{1} + \gamma^C\mathbf{e}_{ij}\mathbf{e}_{ij}\right)\cdot\mathbf{v}_{ij} = -\gamma^T\mathbf{v}_{ij} - \gamma^C(\mathbf{v}_{ij}\cdot\mathbf{e}_{ij})\,\mathbf{e}_{ij}. \tag{6.3.27}$$

The first term on the right-hand side provides the main viscous contribution. The second term is identical in form to the central dissipative force of standard DPD introduced in section 6.2.1. To satisfy the fluctuation-dissipation balance, the following random interaction force ensuring $3\gamma^C > \gamma^T$ is used,

$$\mathbf{F}_{ij}^{R}\mathrm{d}t = (2k_BT)^{1/2}\left((2\gamma^T)^{1/2}\mathrm{d}\overline{\mathbf{W}_{ij}^{S}} + (3\gamma^C-\gamma^T)^{1/2}\frac{1}{3}\,\mathrm{tr}[\mathrm{d}\mathbf{W}_{ij}]\,\mathbf{I}\right)\cdot\mathbf{e}_{ij}. \tag{6.3.28}$$

These stipulations for the dissipative and the random forces in combination with an elastic spring constitute a mesoscopic viscoelastic spring.

To relate the membrane shear viscosity, η_m, to the model dissipative parameters γ^T and γ^C, an element of the hexagonal network shown in figure 6.3.2 is subjected to a constant shear rate, $\dot{\gamma}$. The shear stress τ_{xy} at short times can be approximated from the contribution of the dissipative force in (6.3.27),

$$\begin{aligned} \tau_{xy} = -\frac{1}{2A_0}\Big[&\gamma^T\dot{\gamma}\left((r_y^1)^2 + (r_y^2)^2 + (r_y^2 - r_y^1)^2\right) \\ &+\frac{\gamma^C\dot{\gamma}}{l_0^2}\Big(\,(r_x^1r_y^1)^2 + (r_x^2r_y^2)^2 + (r_x^2 - r_x^1)^2(r_y^2 - r_y^1)^2\,\Big)\Big] \\ &= \dot{\gamma}\,\sqrt{3}\,(\gamma^T + \frac{1}{4}\,\gamma^C\,). \end{aligned} \tag{6.3.29}$$

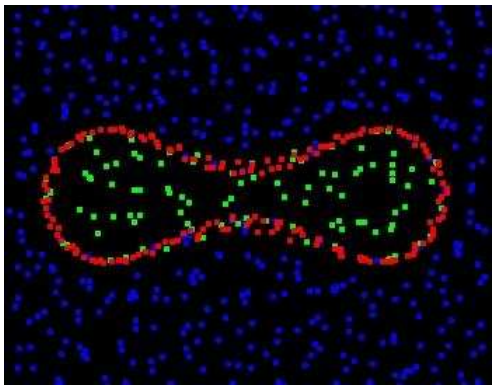

Figure 6.4.1 A slice through a sample equilibrium simulation. Red particles are membrane vertices, blue particles represent the external fluid, and green particles represent the internal fluid. *(Color coded in the electronic file.)*

The membrane viscosity is given by

$$\eta_m = \frac{\tau_{xy}}{\dot{\gamma}} = \sqrt{3}\,(\gamma^T + \frac{1}{4}\,\gamma^C). \tag{6.3.30}$$

As stated in section 6.2.1, simulations with the central viscous force alone corresponding to $\gamma^T = 0$ indicate that γ^T accounts for the largest portion of the membrane dissipation. Accordingly, the numerical results are insensitive to the value of γ^C. Since large values lead to numerical instability, γ^C is set to its minimum value, $\frac{1}{3}\,\gamma^T$, in the simulations.

6.4 Membrane-solvent interfacial conditions

The cell membrane encloses a viscous fluid and is surrounded by a liquid solvent. Figure 6.4.1 shows a snapshot of a simulation at equilibrium. where red particles are membrane vertices, blue particles represent the external fluid, and green particles represent the internal fluid. To prevent mixing of the internal and external fluids, we require impenetrability and enforce adherence or no-slip implemented by pairwise interactions between fluid particles and membrane nodes.

Bounce-back reflection of fluid particles at the triangular plaquettes satisfies membrane impenetrability and better enforces no-slip compared to specular reflection. However, bounce-back reflection alone does not guarantee no-slip, nor does it suppress large unphysical density fluctuations. Fluid

particles whose centers are located at a distance less than a cutoff radius, r_c, require special treatment to account for interactions in the spherical cap lying outside the fluid domain. In practice, this necessitates the DPD dissipative force coefficient between fluid particles and membrane vertices to be properly set (e.g., Fedosov 2010).

The continuum linear shear flow over a flat plate is used to determine the dissipative force coefficient γ for the fluid in the vicinity of the membrane. For the continuum, the total shear force on area A of the plate is $A\eta\dot{\gamma}$, where η is the fluid viscosity and $\dot{\gamma}$ is the local shear-rate. To mimic the membrane surface, wall particles are distributed over the plate to match the configuration of the cell network model. The force on a single wall particle in this system exerted by the surrounding fluid under shear can be expressed as

$$F_v = \iiint_{V_h} n\, g(r)\, F^D \, \mathrm{d}V, \tag{6.4.1}$$

where F^D is the DPD dissipative force between fluid and wall particles, n is the fluid number density, $g(r)$ is the radial distribution function of fluid particles relative to the wall particles, and V_h is the half-sphere volume of fluid above the plate. Thus, the total shear force on the area A is equal to $N_A F_v$, where N_A is the number of plate particles residing in the area A. When conservative interactions between fluid particles and the membrane vertices are neglected, the radial distribution function simplifies to $g(r) = 1$.

Setting $N_A F_v = A\eta\dot{\gamma}$ yields an expression for the dissipative force coefficient γ in terms of the fluid density and viscosity and the wall density, N_A/A. Near a wall where the half-sphere lies within the range of the linear wall shear flow, the shear rate cancels out. This formulation has been verified to enforce satisfactory no-slip boundary conditions without unacceptable wall density fluctuations for the linear shear flow over a flat plate, and is an excellent approximation for no-slip at the membrane surface.

6.5 Numerical and physical scaling

The dimensionless constants and variables in the DPD model must be scaled with physical units. The characteristic length scale r^M is based on the cell diameter at equilibrium, D_0^M, where $[D_0^M] = r^M$ and the superscript M denotes model units. The equilibrium spring length, ℓ_0^M, appears to be too small a scale since the cell dimensions depend generally on the relative volume-to-area ratio. For example, although a red blood cell and a spherical capsule with the same volume may have different surface areas, but they may still have the same ℓ_0^M after triangulation. If the volume-to-area ratio is fixed, D_0^M is proportional to ℓ_0^M.

The length scale adopted in the present work is

$$r^M = \frac{D_0^P}{D_0^M}\,[m], \tag{6.5.1}$$

where the superscript P denotes physical units, and $[m]$ stands for meters. Young's modulus is used as an additional scaling parameter. An energy unit scale can be derived by equating the model and physical Young's moduli,

$$Y^M\,\frac{(k_BT)^M}{(r^M)^2} = Y^P\,\frac{(k_BT)^P}{m^2}, \tag{6.5.2}$$

yielding the model energy scale,

$$(k_BT)^M = \frac{Y^P}{Y^M}\frac{(r^M)^2}{m^2}(k_BT)^P = \frac{Y^P}{Y^M}\left(\frac{D_0^P}{D_0^M}\right)^2(k_BT)^P. \tag{6.5.3}$$

Once the model energy unit is defined, the membrane bending rigidity can be expressed in energy units. With the above length and energy scales, the force scale for membrane stretching is given by

$$N^M = \frac{(k_BT)^M}{r^M} = \frac{Y^P}{Y^M}\frac{D_0^P}{D_0^M}\frac{(k_BT)^P}{m} = \frac{Y^P}{Y^M}\frac{D_0^P}{D_0^M}N^P. \tag{6.5.4}$$

Membrane rheology and dynamics require a time scale in addition to the scales previously defined. A general model time scale is defined as

$$\tau = \frac{t_i^P}{t_i^M}s = \left(\frac{D_0^P}{D_0^M}\frac{\eta_o^P}{\eta_o^M}\frac{Y_0^M}{Y_0^P}\right)^\alpha s, \tag{6.5.5}$$

where η_o is the exterior fluid viscosity and α is a chosen scaling exponent similar to the power-law exponent in rheology.

6.6 Membrane mechanics

The mechanical properties of cell membranes are typically measured by deformation experiments using either micropipette aspiration techniques or optical tweezers (e.g., Evans 1983, Discher *et al.* 1994, Henon *et al.* 1999, Suresh *et al.* 2005). It has been estimated that the shear modulus μ_0 of a healthy RBC lies in the range 2 – 12 μN/m, and the bending rigidity k_c lies in the range 1×10^{-19} – 7×10^{-19} J corresponding to 25–171 k_BT at room temperature 23°C.

To set the mechanical properties of the network model, triangulation of the cell shape described by equation (6.2.15) is first performed yielding an

equilibrium spring length

$$\ell_0 = \frac{1}{N_s} \sum_{i=1}^{N_s} \ell_0^i. \tag{6.6.1}$$

A shear modulus of a healthy cell provides us with a scaling base, $\mu_0 = \mu_0^M$. The WLC spring model requires setting the maximum extension length, ℓ_m^M. However, it is more convenient to set the ratio $x_0 = \ell_0^M/\ell_m^M$ governing the cell nonlinear response at large deformation. The ratio x_0 is fixed at 2.2 in all simulations (e.g., Fedosov 2010).

Necessary model parameters can be calculated from (6.3.9) for given values of ℓ_0^M, μ_0^M, and x_0, thereby circumventing manual adjustment. The calculation of the areal compression modulus K^M and Young's modulus Y^M follows from equations (6.3.13, 6.3.15). for specified area constraint parameters k_a and k_d. In the simulations, we use $\mu_0^M = 100$, $k_a = 4900$, $k_d = 100$, and $k_v = 5000$. We note that the global areal compression and volume constraints are strong, while the local area constraint is weak. The bending rigidity k_c is set to $58(k_BT)^M$ corresponding to physical units 2.4×10^{-19} J at room temperature. The exponent m in relation (6.2.8) is set to 2.

6.6.1 Equilibrium shape and the stress-free model

After initial setup, an equilibrium simulation is run to confirm that the cell retains the biconcave shape. Figure 6.6.1(a) shows an equilibrated shape computed with the WLC-C and the WLC-POW model using typical red blood cell parameters. If all springs have the same equilibrium length, a network on a non-developable surface cannot be constructed with triangles having the same edge lengths. Consequently, the cell surface would necessarily develop local bumps manifested as stress anomalies at the level of a continuum. In fact, the potential energy relaxation performed during the triangulation process produces triangles with a narrow distribution of spring lengths around a specified equilibrium value. Accordingly, a network constructed without annealing implemented by further energy relaxation of the equilibrium shape would still display pronounced bumps and would fail to relax to an equilibrium stress-free axisymmetric shape.

The relaxed cell shape is affected by the ratio of the membrane modulus of elasticity to the bending rigidity expressed by the Föppl-von Kármán number

$$\kappa = \frac{Y_0 R_0^2}{k_c}, \tag{6.6.2}$$

where $R_0 = \sqrt{\pi A_0/4}$. Figure 6.6.1 (b) displays an equilibrated shape computed with the WLC-C or WLC-POW model. The bending rigidity is ten

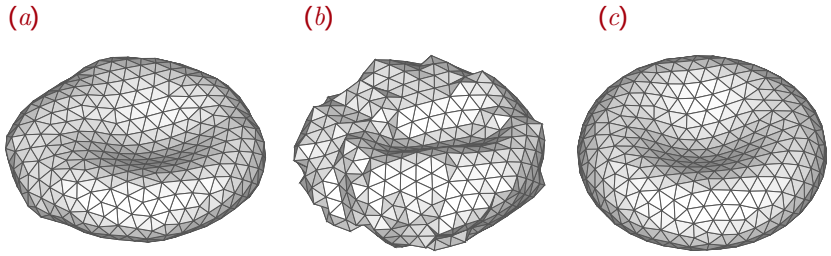

Figure 6.6.1 Equilibrium shape of a cell computed with the WLC-C or WLC-POW model for (*a*) $k_c = 2.4 \times 10^{-19}$ J and (*b*) $k_c = 2.4 \times 10^{-20}$ J. (*c*). Equilibrium shape with the WLC-POW stress-free model for $k_c = 2.4 \times 10^{-20}$ J.

times lower than that of the red blood cell membrane, $k_c = 2.4 \times 10^{-19}$ J. Membrane stress artifacts are significantly pronounced under these conditions.

Shape regularization

A stress-free shape eliminating membrane stress anomalies is obtained by computational annealing. For each spring, the equilibrium spring length ℓ_0^i is adjusted to be the edge length after triangulation, while the ratio x_0 is kept constant at 2.2, for $i = 1, \ldots, N_s$. The maximum spring extension is then set individually to $\ell_m^i = l_0^i \times x_0$. The initial cell network defines local areas for each triangular plaquette, A_0^j, for $j = 1, \ldots, N_t$. The total cell surface area,

$$A_0^{tot} = \sum_{j=1}^{N_t} A_0^j, \tag{6.6.3}$$

and the total cell volume, V_0^{tot}, are calculated from the triangulation. After this adjustment, a new network that is virtually free of irregularities appears. A stretching test along a diameter repeated along several diameters is used to verify that the red cell model behaves like a transversely isotropic body, as discussed in the next section.

The annealing process disqualifies the WLC-C model. The reason is that the assumed isotropic in-plane area-expansion potential expressed by the last term in (6.2.7) is not able to accommodate individual equilibrium spring lengths for each triangle side. Because the POW potential is defined in terms of spring length, it is endowed with the necessary degrees of freedom for equilibrium length adjustment. The individual spring parameters p^i and k_s^i of the WLC-POW model are recalculated based on ℓ_0^i, ℓ_m^i, μ_0^M using (6.3.9) in

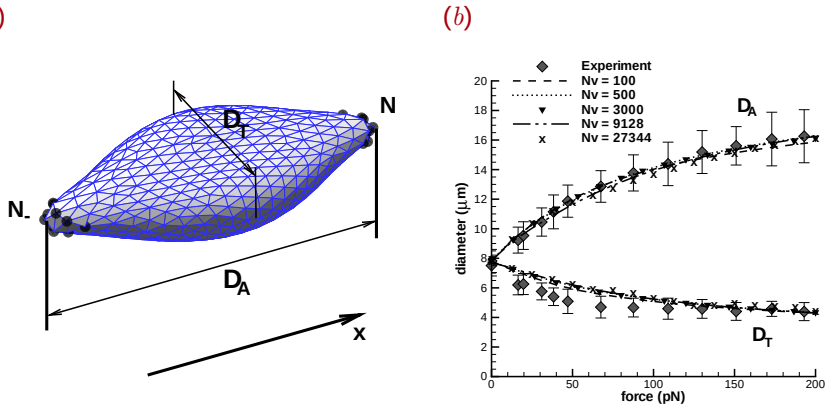

Figure 6.6.2 (a) Schematic illustration of cell deformation. (b) Stretching response with the WLC-POW stress-free model for different coarse-graining levels or number of vertices N_v in the network representation. The diamonds represent experimental results by Suresh *et al.* (2005).

conjunction with the relation $f_{WLC} = f_{POW}$ for the given spring equilibrium length.

Figure 6.6.1(c) shows an equilibrium shape computed with the WLC-POW stress-free model for bending rigidity $k_c = 2.4 \times 10^{-20}$ J. Because membrane stress artifacts are eliminated, arbitrary surface networks can be employed even for small flexural stiffness. However, if the generated network departs too much from a regular hexagonal triangulation, the analytic formulas used to estimate the network macroscopic properties are no longer be reliable.

Stretching test

The reconstructed cell is subjected to stretching analogous to that imposed on cells in optical tweezers experiments (Suresh *et al.* 2005). A stretching force F_s^P up to 200 pN is applied to the outermost $N_+ = \epsilon N_v$ vertices with the largest x coordinates in the positive x direction, and to the outermost $N_- = N_+$ vertices with the smallest x coordinates in the negative x direction, as shown in figure 6.6.2(a). The vertex fraction ϵ is set to 0.02, corresponding to contact diameter of an attached silica bead $d_c = 2$ μm used in the experiments.

For each external force, the cell is allowed to relax to an equilibrium stretched state. The axial diameter, D_A, defined as the maximum distance

between the sets of points N_+ and N_-, and the transverse diameter, D_T, defined as the maximum distance between two points from the set of all vertices projected on a plane perpendicular to the axial diameter, are averaged during a specified simulation time. Results presented in figure 6.6.2(b) are in good agreement with experimental data for all levels of coarse graining. Noticeable discrepancies for the transverse diameter are observed inside the error bars due to experimental error. The optical measurements were performed from a single observation angle. Numerical simulations show that stretched cells may rotate in the yz plane. Consequently, measurements from a single observation angle are likely to underpredict the maximum transverse diameter.

6.7 Membrane rheology from twisting torque cytometry

Early measurements of cell relaxation time employed a micropipette technique to study cell extension and recovery (e.g., Hochmuth *et al.* 1979). The relaxation time extracted from an exponential fit of cell recovery after deformation is on the order of 0.1 s. However, since the deformation is inherently nonuniform in these experiments, it is doubtful that the global technique produces an accurate characteristic membrane time scale (e.g., Yoon *et al.* 2008, Fedosov 2010).

In recent experiments, Puig-de-Morales-Marinkovic *et al.* (2007) applied optical magnetic twisting cytometry (OMTC) to infer a dynamic complex modulus of the cell membrane. In this procedure, the cell membrane response is measured locally by observing the motion of an attached ferromagnetic microbead driven by an oscillating magnetic field. The experiments have confirmed that the membrane is a viscoelastic material. Our viscoelastic membrane model will be tested against the results of optical magnetic twisting cytometry. The numerical simulations emulate the aforementioned experiments where the motion of a microbead attached to the flat side of the biconcave cell due an oscillating torque is studied, as shown in figure 6.7.1(a). The data allow us to infer membrane properties such as the complex modulus.

In the numerical model, the microbead is represented by a set of vertices deployed on a rigid sphere. A group of cell vertices near the bottom of the microbead simulates the area of attachment. The torque on the microbead is applied only to the bead vertices. Figure 6.7.1(b) presents a typical response to an oscillating torque. The bead motion, monitored by the displacement of the center of mass, oscillates with the applied torque frequency. The oscillation is shifted by a phase angle, ϕ, that depends on the applied frequency. In the case of a purely elastic material and in the absence of inertia, the phase angle ϕ would be zero zero for any torque frequency.

The linear complex modulus of a viscoelastic material can be extracted

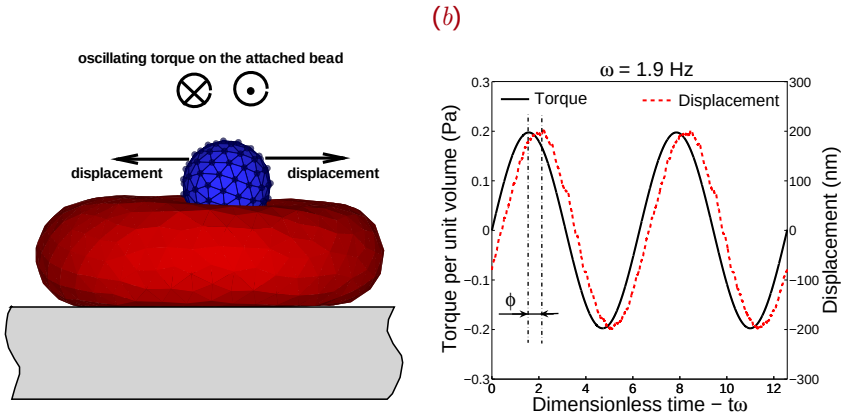

Figure 6.7.1 (*a*) Illustration of the numerical setup of the twisting torque cytometry. (*b*) Response of an attached microbead subject to an oscillating torque exerted on the bead.

from the phase angle and torque frequency using the relations

$$g'(\omega) = \frac{\Delta T}{\Delta d}\cos\phi, \qquad g''(\omega) = \frac{\Delta T}{\Delta d}\sin\phi, \tag{6.7.1}$$

where $g'(\omega)$ and $g''(\omega)$ are two-dimensional storage and loss moduli and ΔT and Δd are the torque and bead displacement amplitudes. In the absence of inertia, the phase angle ϕ ranges between 0 and $\pi/2$.

Figure 6.7.2 compares the computed complex modulus with experimental data by Puig-de-Morales-Marinkovic *et al.* (2007). Good agreement is found for bending rigidity $k_c = 4.8 \times 10^{-19}$ J and membrane viscosity $\eta_m = 0.022$ Pa s. Numerical twisting cytometry suggests that the storage modulus behaves as

$$g'(\omega) \sim (k_c Y_0)^{0.65}. \tag{6.7.2}$$

Since the Young modulus of healthy cells is fixed by the cell stretching test, figure 6.7.2 essentially illustrates the dependence of g' on the membrane bending rigidity. To ensure good agreement with experiments, the bending rigidity of a healthy cell must be in the range 4 to 5×10^{-19} J, which is twice the widely adopted value, $k_c = 2.4 \times 10^{-19}$ J.

For small displacements, the loss modulus g'' depends mainly on the surface viscosity and is insensitive to the membrane's elastic properties. The simulated loss modulus follows a power law in frequency with exponent $\alpha =$

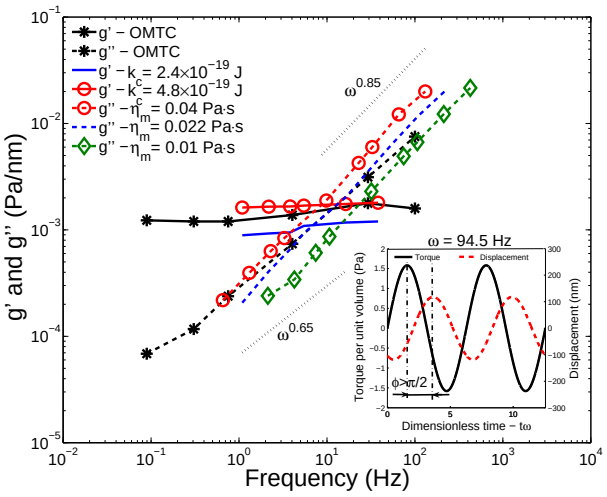

Figure 6.7.2 Graphs of the functions g' and g'' obtained from simulations with different membrane viscosities and bending rigidities. The numerical results are compared with experimental data by Puig-de-Morales-Marinkovic *et al.* (2007). The inset illustrates the effect of inertia for high frequencies of the driving torque.

0.85 to be used in (6.5.5). In the experiments, the exponent is approximately 0.75. The agreement is fair in view of fitting errors in only two frequency decades in simulation and experiment. The inset in figure 6.7.2 shows that inertial effects affect g' at high frequencies. Decreasing the bead mass would allow us to obtain rheological data for higher torque frequencies, but the computational cost is high since a small time step is required. When the loss modulus dominates the storage modulus, the bead-displacement amplitude at fixed torque amplitude is extremely small and hard to measure in the laboratory. However, bead displacements in simulations can be successfully detected on a scale of several nanometers.

6.8 Deformation in shear flow

Experimental observations have shown that red blood cells tumble at low shear rates and exhibit a tank-treading motion at high shear rates (e.g., Tran-Son-Tay *et al.* 1984, Fischer 2004, 2007, Abkarian *et al.* 2007). Fischer (2004) attributed this behavior to a minimum elastic energy state of the cell membrane. Cells can be made to tank-tread in the laboratory for several hours.

When the flow is stopped, the cells relax to the original biconcave shape where attached microbeads recover their original relative position. It appears that tank-treading is possible only when a certain elastic energy barrier has been surpassed. Theoretical analyses have considered ellipsoidal cell models tank-treading along a fixed ellipsoidal path (e.g., Abkarian *et al.* 2007, Skotheim & Secomb 2007). Our simulations show that the dynamics depends on the membrane shear modulus, shear rate, and viscosity ratio $\lambda = (\eta_i + \eta_m)/\eta_o$, where η_i, η_m, and η_o are the interior, membrane, and outer fluid viscosities.

For viscosity ratio $\lambda < 3$, the theory predicts tumbling at low shear rates and tank-treading motion at high shear rates (e.g., Skotheim & Secomb 2007). The cells exhibit an unstable behavior in a narrow intermittent region around the tumbling-to-tank-treading transition where tumbling can be followed by tank-treading and *vice versa.* For $\lambda > 3$, stable tank-treading does not necessarily arise. Red blood cells with viscosity ratio $\lambda > 3$ have been observed to tank-tread while exhibiting a swinging motion with a certain frequency and amplitude about an average tank-treading axis. The reliability of the theoretical predictions will be judged by comparison with the results of our simulations.

In the first simulation, a cell is suspended in a linear shear flow between two parallel walls. The viscosities of the external solvent and internal cytosol fluid are set to $\eta_o = \eta_i = 0.005$ Pa s. Consistent with results of twisting torque cytometry, the membrane viscosity is set to $\eta_m = 0.022$ Pa s. Figure 6.8.1 presents information on the cell tumbling and tank-treading frequencies under different conditions. Experimental observations by Tran-Son-Tay *et al.* (1984) and Fischer (2007) are included for comparison.

In the case of a purely elastic membrane with or without inner solvent (circles and squares), the numerical results significantly overpredict the tank-treading frequency compared with experimental measurements. The internal solvent viscosity could be further increased to improve agreement with experimental data. However, since the cytosol is a hemoglobin solution with a well-defined viscosity of about 0.005 Pa s, excess viscous dissipation must occur inside the membrane (e.g., Cokelet and Meiselman 1968). The data plotted with triangles in figure 6.8.1 show good agreement with experimental data for increased membrane viscosity.

The tumbling frequency is nearly independent of the medium viscosities. Increasing the viscosity of the internal fluid or raising the membrane viscosity slightly shifts the tumbling-to-treading threshold into higher shear rates through an intermittent regime. We estimate that the tank-treading energy barrier of a cell is approximately $E_c = 3$ to 3.5×10^{-17} J . In a theoretical model proposed by Skotheim & Secomb (2007), the energy barrier was

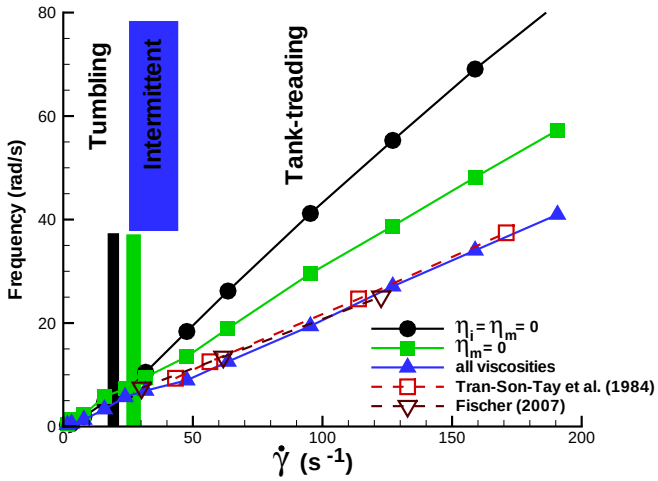

Figure 6.8.1 Tumbling and tank-treading frequency of a RBC in shear flow for $\eta_o = 0.005$ Pa s, $\eta_i = \eta_m = 0$ (circles); $\eta_o = \eta_i = 0.005$ Pa s, $\eta_m = 0$ (squares); $\eta_o = \eta_i = 0.005$ Pa s, $\eta_m = 0.022$ Pa s (triangles).

set to $E_c = 10^{-17}$ J to ensure agreement with experimental data. Membrane deformation during tank treading is indicated by an increase in the elastic energy difference with increasing shear rate to within about 20% of E_c.

An intermittent regime is observed with respect to the shear rate in all cases. Consistent with the experiments, the width of the transition zone broadens as the membrane viscosity increases. Similar results regarding intermittency were reported by Kessler *et al.* (2008). for viscoelastic vesicles. We conclude that theoretical predictions of cell dynamics in shear flow are qualitative correct at best due to the assumption of ellipsoidal shape and fixed ellipsoidal tank-treading path. Experiments by Abkarian *et al.* (2007) have shown and the present simulations have confirmed that the cell deforms along the tank-treading axis with strains of order $0.1 - 0.15$.

Cell deformation in shear flow depends on the ratio of the membrane elastic to bending modulus, expressed by the Föppl-von Kármán number κ defined in (6.6.2). Figures 6.8.2 (a) and (b) show several snapshots of tumbling and tank-treading cells with bending rigidity set to ten times that commonly used for red blood cells, $k_c = 2.4 \times 10^{-18}$ J, corresponding to Föppl-von Kármán number $\kappa = 85$. Tumbling to tank-treading transition occurs at shear

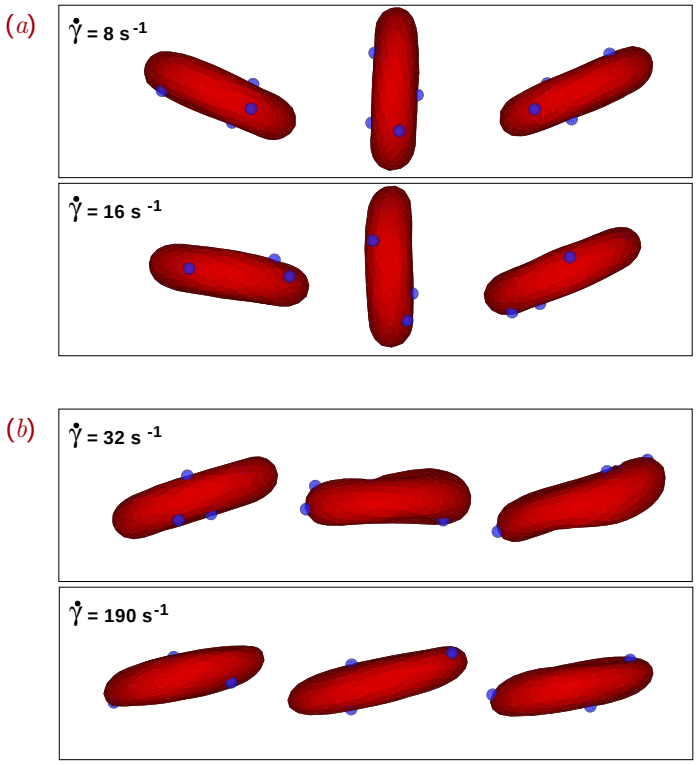

Figure 6.8.2 Snapshots of (a) a tumbling and (b) a tank-treading cell at different shear rates, for viscosities $\eta_o = \eta_i = 0.005$ Pa s, $\eta_m = 0.022$ Pa s, bending rigidity $k_c = 2.4 \times 10^{-18}$ J, and Föppl-von Kármán number $\kappa = 85$. Blue particles are added as tracers during post-processing for visual clarity. (*Color in the electronic file.*)

rates 20–25 s^{-1}. The results show negligible deformation during tumbling and small deformation during tank-treading following the transition.

Figure 6.8.3 presents analogous results for tumbling and tank-treading cells with bending rigidity $k_c = 2.4 \times 10^{-19}$ J corresponding to $\kappa = 850$. Significant shape deformation is observed during tumbling and tank-treading. However, the frequency of the motion is hardly changed from that corresponding to $\kappa = 85$. Since the discrete network cannot adequately capture the membrane bending on length scales comparable to the element size, a further decrease of the bending rigidity results in buckling. To screen out the effect of the membrane discretization, simulations were performed with $Nv = 1000$ and 3000 membrane network vertices and similar results were

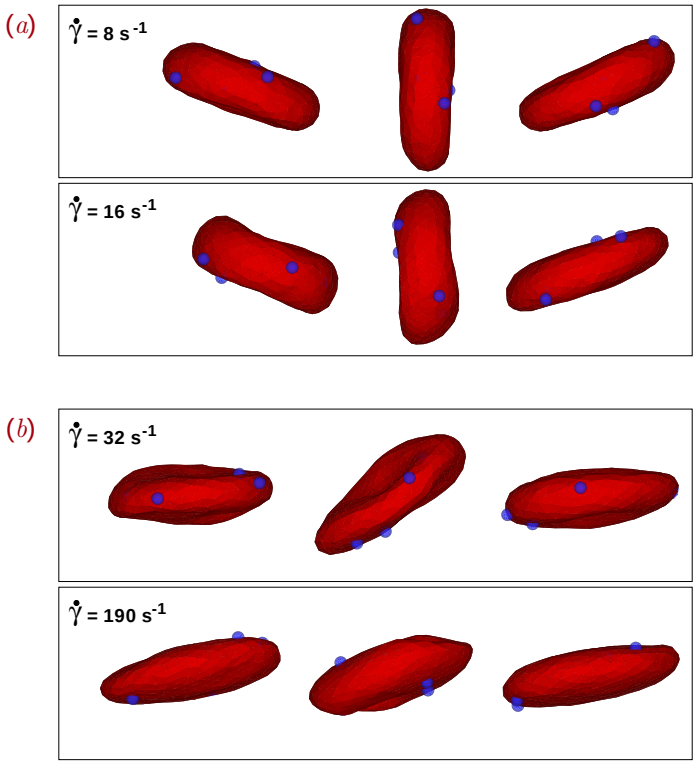

Figure 6.8.3 Snapshots of (a) a tumbling and (b) a tank-treading cell at different shear rates for viscosity $\eta_o = \eta_i = 0.005$ Pa s, $\eta_m = 0.022$ Pa s, bending rigidity $k_c = 2.4 \times 10^{-19}$ J, and Föppl-von Kármán number $\kappa = 850$. Blue particles are added as tracers during post-processing for visual clarity. (*Color in the electronic file.*)

obtained for corresponding Föppl-von Kármán numbers.

The simulations suggest that the membrane bending rigidity is several times larger than the widely accepted value $k_c = 2.4 \times 10^{-19}$ J. Simulations of twisting torque cytometry presented previously in this chapter corroborate this assertion. An increase in the membrane shear modulus raises the Föppl-von Kármán number and the tank-treading energy barrier E_c, and hence also shifts the tumbling-to-tank-treading transition to higher shear rates.

We have seen that a cell oscillates or swings around tank-treading axes with a certain frequency and amplitude, as shown in figures 6.8.2 and 3. Figure 6.8.4 presents graphs of the average tank-treading angle and swinging

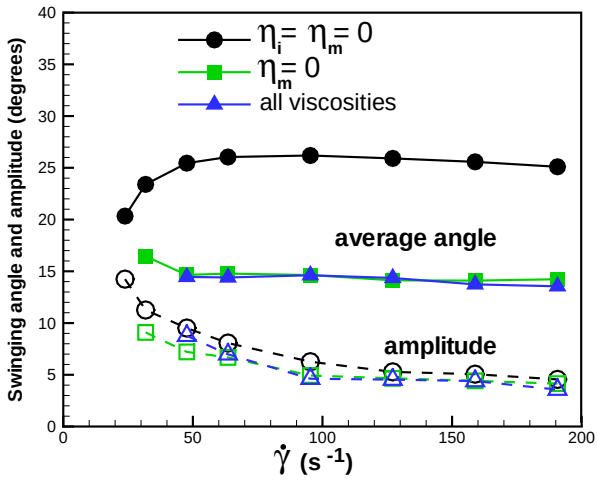

Figure 6.8.4 Graphs of the swinging average angle in degrees (filled symbols) and amplitude (open symbols) for (*a*) $\eta_o = 0.005$ Pa s and $\eta_i = \eta_m = 0$ (circles); (*b*) $\eta_o = \eta_i = 0.005$ Pa s and $\eta_m = 0$ (squares); (*c*) $\eta_o = \eta_i = 0.005$ Pa s and $\eta_m = 0.022$ Pa s (triangles).

amplitude. The numerical results are consistent with experimental data by Abkarian *et al.* (2007). The average swinging angle is larger for a purely elastic membrane without inner cytosol. The inclination angle is independent of the internal fluid and membrane viscosities and the swinging amplitude is insensitive to the fluid and membrane properties. The swinging frequency is exactly twice the tank-treading frequency.

6.9 Tube flow

The mean velocity of Poiseuille flow in a circular tube is defined as

$$\bar{v} = \frac{1}{S} \iint v(r)\, \mathrm{d}S, \tag{6.9.1}$$

where S is the cross-sectional area and $v(r)$ is the axial velocity. For a Newtonian fluid, $\bar{v} = v_c/2$, where v_c is the centerline velocity.

At low flow rates, a cell suspended in tube flow retains its biconcave shape. As the driving pressure gradient increases, the cell obtains the parachute-like shape shown in figure 6.9.1 for a tube with diameter $9\mu m$, in

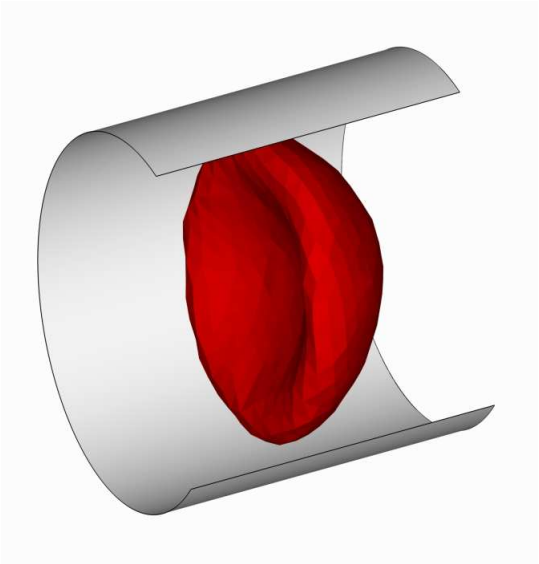

Figure 6.9.1 Parachute shape of a cell suspended in Poiseuille flow through a 9μm diameter tube.

agreement with experimental observations (e.g., Tsukada *et al.* 2001). To identify the biconcave-to-parachute transition, we compute the gyration tensor

$$G_{mn} = \frac{1}{N_v} \sum_i (r_m^i - r_m^C)(r_n^i - r_n^C), \tag{6.9.2}$$

where $\mathbf{r}^i$ are the membrane vertex coordinates, $\mathbf{r}^C$ is the membrane center of mass, and m, n stand for x, y, or z. (e.g., Mattice & Suter 1994). The eigenvalues of the gyration tensor allow us to accurately characterize the cell shape. For the equilibrium biconcave shape, the gyration tensor has two large eigenvalues corresponding to the midplane of the biconcave disk, and one small eigenvalues corresponding to the disk thickness. At the biconcave-to-parachute transition, the small eigenvalue increases indicating that the cell elongates along the tube axes.

Figure 6.9.2 illustrates the dependence of the axial eigenvalue on the mean flow velocity for different membrane bending rigidities and shear moduli. The dashed line describes the biconcave-to-parachute transition. For healthy cells, the transition occurs at a mean velocity of about 65 μm/s. The transition occurs at larger bending rigidity or membrane shear modulus at

(*a*) (*b*)

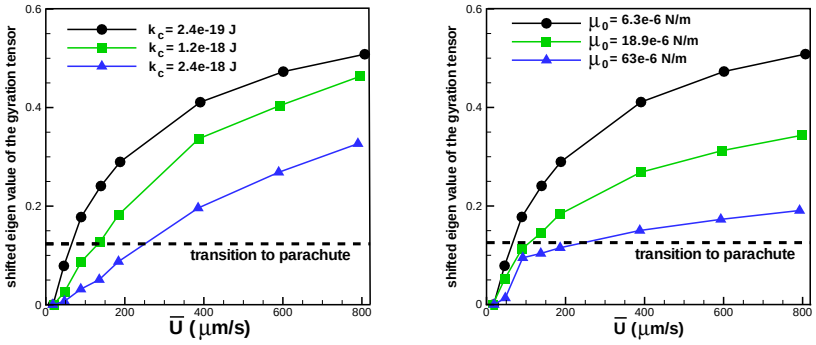

Figure 6.9.2 Excess axial eigenvalue of the gyration tensor above that for a biconcave disk for (*a*) different bending rigidities and (*b*) different membrane shear moduli. The cell volume fraction is $C = 0.05$.

stronger flows. The critical mean velocity changes almost linearly with the bending rigidity, k_c, and shear modulus, μ_0. These results are consistent with numerical simulations by Noguchi & Gompper (2005). Stiffer capsules suffer smaller elongation along at the same mean velocity. The results in figure 6.9.2 corroborate the notion that stiffer cells exhibit stronger resistance to flow.

The relative apparent viscosity of the suspension is defined as

$$\lambda_{app} = \frac{\eta_{app}}{\eta_o}, \qquad \eta_{app} = \frac{nfR_0^2}{8\bar{u}}, \tag{6.9.3}$$

where n is the cell number density, f is the force exerted on each cell, R_0 is the tube radius, η_o is the solvent viscosity, and $\bar{u}$ is the bulk velocity calculated using equation (6.9.1). The product nf is the streamwise pressure gradient, $\Delta P/L$, where L is the tube length. Figure 6.9.3 reveals a slight increase in the apparent viscosity with cell stiffening due to increased flow resistance. The effect is small even for a tenfold increase in the membrane elastic modulus due to the low cell concentration, $C = 0.05$. A stronger effect is expected at at higher volume fractions.

6.10 Summary

We have presented a mesoscopic model of red blood cells implemented by the dissipative particle dynamics (DPD) method. The spectrin cytoskeleton is represented by a network of interconnected viscoelastic springs comprising a

(*a*) (*b*)

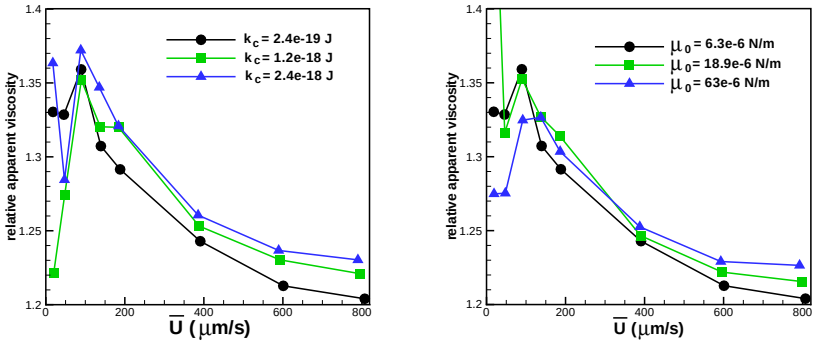

Figure 6.9.3 Relative apparent viscosity for (*a*) different bending rigidities and (*b*) different membrane shear moduli. The cell volume fraction is $C = 0.05$.

membrane with elastic and viscous properties. The surface network accounts for bending resistance attributed to the lipid bilayer and incorporates local and global area constraints to ensure constant volume and surface area. The model was validated by a number of tests on membrane mechanics, rheology, and cell dynamics in shear and Poiseuille flow.

The macroscopic properties of the membrane were related to the network parameters by theoretical analysis. The predicted mechanical properties of the cells agree with optical tweezers experiments even for a highly coarse-grained membrane representation with respect to the number of vertices in the spectrin network. Cell rheology was probed by numerical experiments simulating twisting torque cytometry. The predicted membrane viscosity is consistent with the experimental value 0.022 Pa s, which is about twenty two times that of water. The numerical results indicate that the bending rigidity of the the membrane can be two to three times higher than the widely accepted value $k_c = 2.4 \times 10^{-19}$ J.

Red blood cell deformation was simulated in shear and Poiseuille flow. In shear flow, a cell exhibits tumbling at low shear rates and tank-treading at high shear rates. A narrow intermittent region appears where these modes interchange. The theoretical model is able to quantitatively capture cell dynamics in shear flow. Comparison of the numerical results with existing theoretical predictions suggest that the latter suffers from oversimplification . Near the tumbling-to-tank-treading transition, simulated cells exhibit strong deformation. The cell bending rigidity is estimated to be several times the

accepted value of $k_c = 2.4 \times 10^{-19}$ J. Further experimental data on cell deformations around the tumbling-to-tank-treading transition could confirm the complex dynamics observed in the simulations. Simulations of cell motion in Poiseuille flow through a 9 μm diameter tube demonstrated a transition to a parachute shape at a mean velocity of about 65 μm/s. The threshold occurs at higher mean velocities for stiffer cells with a higher bending rigidity or shear modulus.

Most of the current cell models assume that the cell membrane is purely elastic. The simulations described in this chapter show that membrane viscosity is essential for capturing single cell rheology and dynamics. The presented model is general enough to be used with other simulation methods, including Lattice-Boltzmann, Brownian dynamics, the immersed-boundary method, and multiparticle collision dynamics.

Acknowledgement

This work was supported by the NSF grant CBET-0852948 and by the NIH grant R01HL094270. Computations were performed at the NSF NICS facility.

Appendix

The modeled membrane is described by the potential energy $V(\{\mathbf{x}_i\})$ given in (6.2.6)) with contributions defined in (6.2.7) – (6.2.13). Nodal forces corresponding to these energies are derived according to equation (6.2.14) and then divided into three parts: two-point interactions mediated by springs defined in (6.2.8) and 6.2.9), three-point interactions representing stored elastic energy and mediating area and volume conservation constraints according to (6.2.7), (6.2.12), and (6.2.13), and four-point interactions implementing flexural stiffness between adjacent faces.

Figure 6A.1(a) shows a sample triangular element of a membrane network. We introduce the distance matrix $\mathbf{a}_{ij} = \mathbf{p}_i - \mathbf{p}_j$, where i and j take the values 1, 2, and 3, and the normal vector $\boldsymbol{\xi} = \mathbf{a}_{21} \times \mathbf{a}_{31}$. The area of the triangle is

$$A_k = \frac{1}{2}\,|\boldsymbol{\xi}| = \frac{1}{2}\,(\xi_x^2 + \xi_y^2 + \xi_z^2)^{1/2}. \tag{6A.1}$$

The stored elastic energy for a single triangle generates the following nodal forces according to (6.2.7),

$$f_{s_i} = -\frac{\partial\,(C_q/A_k^q)}{\partial s_i} = \alpha\big(\xi_x \frac{\partial \xi_x}{\partial s_i} + \xi_y \frac{\partial \xi_y}{\partial s_i} + \xi_z \frac{\partial \xi_z}{\partial s_i}\big), \tag{6A.2}$$

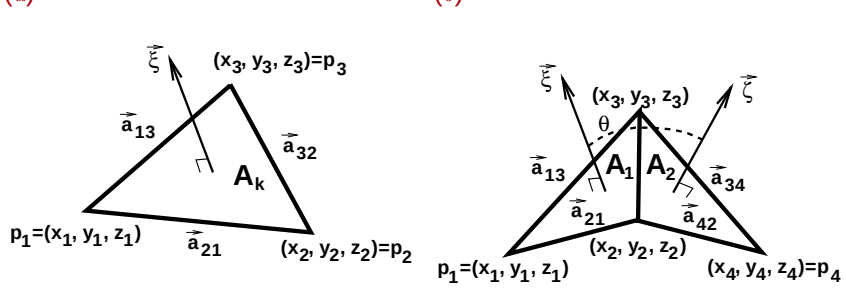

Figure 6A.1 (*a*) Illustration of a triangular element of the surface network, and (*b*) Sketch of two adjacent triangular elements of the network.

where

$$\alpha = 2^q \frac{q\, C_q}{(\xi_x^2 + \xi_y^2 + \xi_z^2)^{q/2+1}} = \frac{q\, C_q}{4 A_k^{q+2}}, \tag{6A.3}$$

s_i stands for x, y, and z, and $i = 1, 2, 3$. Explicitly,

$$\begin{aligned} &(f_{x_1}, f_{y_1}, f_{z_1}) = \alpha\, (\boldsymbol{\xi} \times \mathbf{a}_{32})\,, \qquad (f_{x_2}, f_{y_2}, f_{z_2}) = \alpha\, (\boldsymbol{\xi} \times \mathbf{a}_{13})\,, \\ &(f_{x_3}, f_{y_3}, f_{z_3}) = \alpha\, (\boldsymbol{\xi} \times \mathbf{a}_{21})\,. \end{aligned} \tag{6A.4}$$

The global area conservation constraint represented by the first term on the right-hand side of (6.2.12) produces the nodal forces

$$\begin{aligned} f_{s_i} &= -\frac{\partial}{\partial s_i}\Big[\frac{k_a (A - A_0^{tot})^2}{2 A_0^{tot}}\Big] = -\frac{k_a (A - A_0^{tot})}{A_0^{tot}} \frac{\partial A}{\partial s_i} = \beta_a \sum_{k=1}^{N_t} \frac{\partial A_k}{\partial s_i} \\ &= \beta_a \sum_{k=1}^{N_t} \frac{1}{4 A_k} \Big(\xi_x^k \frac{\partial \xi_x^k}{\partial s_i} + \xi_y^k \frac{\partial \xi_y^k}{\partial s_i} + \xi_z^k \frac{\partial \xi_z^k}{\partial s_i}\Big), \end{aligned} \tag{6A.5}$$

where $\beta_a = -k_a (A - A_0^{tot})/A_0^{tot}$, the superscript k denotes the kth triangle, and $i = 1, \ldots, N_v$. For a single triangle, the nodal forces have the functional form shown in (6A.4) with $\alpha = \beta_a/(4A_k)$.

For a single triangle, the local area conservation constraint expressed by the second term on the right-hand side of (6.2.12) produces nodal forces given by (6A.4) with $\alpha = -k_d (A_k - A_0)/(4 A_0 A_k)$.

Global volume conservation expressed by (6.2.13) produces the nodal forces

$$f_{s_i} = -\frac{\partial}{\partial s_i}\left[\frac{k_v(V-V_0^{tot})^2}{2V_0^{tot}}\right] = -\frac{k_v(V-V_0^{tot})}{V_0^{tot}}\frac{\partial V}{\partial s_i} = \beta_v \sum_{k=1}^{N_t}\frac{\partial V_k}{\partial s_i}, \tag{6A.6}$$

where $V_k = \frac{1}{6}(\boldsymbol{\xi}^k \cdot \mathbf{t}_c^k)$, and $\mathbf{t}_c^k = (p_1^k + p_2^k + p_3^k)/3$ is the center of mass of the kth triangle shown in figure 6.A.1. The nodal forces for a single triangle arise from the volume constraint as

$$\begin{aligned}
(f_{x_1}, f_{y_1}, f_{z_1}) &= \frac{\beta_v}{6}(\frac{1}{3}\,\boldsymbol{\xi} + \mathbf{t}_c \times \mathbf{a}_{32}),\\
(f_{x_2}, f_{y_2}, f_{z_2}) &= \frac{\beta_v}{6}\,(\frac{1}{3}\,\boldsymbol{\xi} + \mathbf{t}_c \times \mathbf{a}_{13}),\\
(f_{x_3}, f_{y_3}, f_{z_3}) &= \frac{\beta_v}{6}\,(\frac{1}{3}\,\boldsymbol{\xi} + \mathbf{t}_c \times \mathbf{a}_{21}).
\end{aligned} \tag{6A.7}$$

Four-point interactions are encountered in the bending energy between two adjacent faces expressed by (6.2.11). Figure 6A.2(a) shows an arrangement of two adjacent triangular elements in the network. The triangle normal vectors are $\boldsymbol{\xi} = \mathbf{a}_{21} \times \mathbf{a}_{31}$ and $\boldsymbol{\zeta} = \mathbf{a}_{34} \times \mathbf{a}_{24}$, and the corresponding areas are $A_1 = |\boldsymbol{\xi}|/2$, and $A_2 = |\boldsymbol{\zeta}|/2$. Bending energy produces the nodal forces

$$f_{s_i} = -\frac{\partial}{\partial s_i}\left[k_b[1-\cos(\theta-\theta_0)]\right] = -k_b \sin(\theta-\theta_0)\frac{\partial \theta}{\partial s_i}, \tag{6A.8}$$

where θ is the angle subtended between the normals $\boldsymbol{\xi}$ and $\boldsymbol{\zeta}$, given by

$$\cos\theta = (\frac{\boldsymbol{\xi}}{|\boldsymbol{\xi}|} \cdot \frac{\boldsymbol{\zeta}}{|\boldsymbol{\zeta}|}). \tag{6A.9}$$

We write $\sin(\theta-\theta_0) = \sin\theta\cos\theta_0 - \cos\theta\sin\theta_0$, where $\sin\theta = \pm(1-\cos^2\theta)^{1/2}$ taken with the plus sign if $([\boldsymbol{\xi} - \boldsymbol{\zeta}] \cdot [\mathbf{t}_c^1 - \mathbf{t}_c^2]) \geq 0$ and with the minus sign otherwise, where $\mathbf{t}_c^1$ and $\mathbf{t}_c^2$ are the centers of mass vectors of the first and second triangle. The derivative of θ with respect to s_i are given by

$$\frac{\partial \theta}{\partial s_i} = \frac{\partial}{\partial s_i}\arccos(\frac{\boldsymbol{\xi}}{|\boldsymbol{\xi}|} \cdot \frac{\boldsymbol{\zeta}}{|\boldsymbol{\zeta}|}) = -\frac{1}{\sqrt{1-\cos^2\theta}}\frac{\partial}{\partial s_i}(\frac{\boldsymbol{\xi}}{|\boldsymbol{\xi}|} \cdot \frac{\boldsymbol{\zeta}}{|\boldsymbol{\zeta}|}). \tag{6A.10}$$

Analytical calculation of the derivatives produces the following nodal forces due to four-point interactions,

$$\begin{aligned}
(f_{x_1}, f_{y_1}, f_{z_1}) &= b_{11}\,(\boldsymbol{\xi} \times \mathbf{a}_{32}) + b_{12}\,(\boldsymbol{\zeta} \times \mathbf{a}_{32})\,,\\
(f_{x_2}, f_{y_2}, f_{z_2}) &= b_{11}\,(\boldsymbol{\xi} \times \mathbf{a}_{13}) + b_{12}\,(\boldsymbol{\xi} \times \mathbf{a}_{34} + \boldsymbol{\zeta} \times \mathbf{a}_{13}) + b_{22}(\boldsymbol{\zeta} \times \mathbf{a}_{34}),\\
(f_{x_3}, f_{y_3}, f_{z_3}) &= b_{11}\,(\boldsymbol{\xi} \times \mathbf{a}_{21}) + b_{12}\,(\boldsymbol{\xi} \times \mathbf{a}_{42} + \boldsymbol{\zeta} \times \mathbf{a}_{21}) + b_{22}(\boldsymbol{\zeta} \times \mathbf{a}_{42}),\\
(f_{x_4}, f_{y_4}, f_{z_4}) &= b_{12}\,(\boldsymbol{\xi} \times \mathbf{a}_{23}) + b_{22}\,(\boldsymbol{\zeta} \times \mathbf{a}_{23})\,,
\end{aligned} \tag{6A.11}$$

where

$$b_{11} = -\beta_b \cos\theta/|\boldsymbol{\xi}|^2, \quad b_{12} = \beta_b/(|\boldsymbol{\xi}||\boldsymbol{\zeta}|), \quad b_{22} = -\beta_b \cos\theta/|\boldsymbol{\zeta}|^2, \quad (6A.12)$$

and

$$\beta_b = k_b(\sin\theta\cos\theta_0 - \cos\theta\sin\theta_0)/\sqrt{1-\cos^2\theta}. \quad (6A.13)$$

References

ABKARIAN, M., FAIVRE, M. & VIALLAT, A. (2007) Swinging of red blood cells under shear flow. *Phys. Rev. Lett.* **98**, 188302.

ALLEN, M. P. & TILDESLEY, D. J. (1987) *Computer simulation of liquids.* Clarendon Press, New York.

COKELET, G. R. & MEISELMAN, H.J. (1968) Rheological comparison of hemoglobin solutions and erythrocyte suspensions. *Science* **162**, 275–277.

DAO, M., LI, J. & SURESH, S. (2006) Molecularly based analysis of deformation of spectrin network and human erythrocyte. *Materials Sci. Engin. C* **26**, 1232–1244.

DISCHER, D. E., MOHANDAS, N. & EVANS, E. A. (1994) Molecular maps of red cell deformation: hidden elasticity and in situ connectivity. *Science* **266**, 1032–1035.

DISCHER, D. E., BOAL, D. H. & BOEY, S. K. (1998) Simulations of the erythrocyte cytoskeleton at large deformation. II. Micropipette aspiration. *Biophys. J.* **75**, 1584–1597.

DUPIN, M. M., HALLIDAY, I., CARE, C. M., ALBOUL, L. & MUNN, L. L. (2007) Modeling the flow of dense suspensions of deformable particles in three dimensions. *Phys. Rev. E* **75**, 066707.

EGGLETON, C. D. & POPEL, A. S. (1998) Large deformation of red blood cell ghosts in simple shear flow. *Phys. Fluids* **10**, 1834–1845.

ESPANOL, P. (1998) Fluid particle model. *Phys. Rev. E* **57**, 2930–2948.

ESPANOL, P. & WARREN, P. (1995) Statistical mechanics of dissipative particle dynamics. *Europhys. Lett.* **30**, 191–196.

EVANS, E. A. & SKALAK, R. (1980) *Mechanics and Thermodynamics of Biomembranes.* CRC.

Evans, E. A. (1983) Bending elastic modulus of red blood cell membrane derived from buckling instability in micropipette aspiration tests. *Biophys. J.* **43**, 27–30.

Fan, X., Phan-Thien, N., Chen, S., Wu, X. & Ng, T. Y. (2006) Simulating flow of DNA suspension using dissipative particle dynamics. *Phys. Fluids* **18**, 063102.

Fedosov, D. A., Karniadakis, G. E. & Caswell, B. (2008) Dissipative particle dynamics simulation of depletion layer and polymer migration in micro- and nanochannels for dilute polymer solutions. *J. Chem. Phys.* **128**, 144903.

Fedosov, D. A., (2010) *Multiscale Modeling of Blood Flow and Soft Matter.* PhD thesis, Brown University, Providence.

Fischer, T. M. (2004) Shape memory of human red blood cells. *Biophys. J.* **86**, 3304–3313.

Fischer, T. M. (2007) Tank-tread frequency of the red cell membrane: Dependence on the viscosity of the suspending medium. *Biophys. J.* **93**, 2553–2561.

Fung, Y. C. (1993) *Biomechanics: Mechanical Properties of Living Tissues.* Springer-Verlag, New York.

Helfrich, W. (1973) Elastic properties of lipid bilayers: Theory and possible experiments. *Z. Naturforschung C* **28**, 693–703.

Henon, S., Lenormand, G., Richert, A. & Gallet, F. (1999) A new determination of the shear modulus of the human erythrocyte membrane using optical tweezers. *Biophys. J.* **76**, 1145–1151.

Hochmuth, R. M., Worthy, P. R. & Evans, E. A. (1979) Red cell extensional recovery and the determination of membrane viscosity. *Biophys. J.* **26**, 101–114.

Hoogerbrugge, P. J. & Koelman, J. M. V .A. (1992) Simulating microscopic hydrodynamic phenomena with dissipative particle dynamics. *Europhys. Lett.* **19**, 155–160.

Kessler, S., Finken, R. & Seifert, U. (2008) Swinging and tumbling of elastic capsules in shear flow. *J. Fluid Mech.* **605**, 207–226.

Li, J., Dao, M., Lim, C. T. & Suresh, S. (2005) Spectrin-level modeling of the cytoskeleton and optical tweezers stretching of the erythrocyte. *Biophys. J.* **88**, 3707–3719.

LIDMAR, J., MIRNY, L. & NELSON, D. R. (2003) Virus shapes and buckling transitions in spherical shells. *Phys. Rev. E* **68**, 051910.

MALEVANETS, A. & KAPRAL, R. (1999) Mesoscopic model for solvent dynamics. *J. Chem. Phys.* **110**, 8605–8613.

MATTICE, W. L. & SUTER, U. W. (1994) *Conformational theory of large molecules: The rotational isomeric state model in macromolecular systems.* Wiley Interscience, New York.

NOGUCHI, H. & GOMPPER, G. (2005) Shape transitions of fluid vesicles and red blood cells in capillary flows. *Proc. Natl. Acad. Sci. USA* **102**, 14159–14164.

PIVKIN, I. V. & KARNIADAKIS, G. E. (2008) Accurate coarse-grained modeling of red blood cells. *Phys. Rev. Lett.* **101**, 118105.

POZRIKIDIS, C. (2005) Numerical simulation of cell motion in tube flow. *Ann. Biomed. Eng.* **33**, 165–178.

PUIG-DE-MORALES-MARINKOVIC, M., TURNER, K. T., BUTLER, J. P., FREDBERG, J. J. & SURESH, S. (2007) Viscoelasticity of the human red blood cell. *Am. J. Physiol.: Cell Physiol.* **293**, 597–605.

SKOTHEIM, J. M. & SECOMB, T. W. (2007) Red blood cells and other non-spherical capsules in shear flow: Oscillatory dynamics and the tank-treading-to-tumbling transition. *Phys. Rev. Lett.* **98**, 078301.

SUCCI, S. (2001) *The Lattice Boltzmann equation for fluid dynamics and beyond.* Oxford University Press, Oxford.

SURESH, S., SPATZ, J., MILLS, J. P., MICOULET, A., DAO, M., LIM, C. T., BEIL, M. & SEUFFERLEIN, T. (2005) Connections between single-cell biomechanics and human disease states: gastrointestinal cancer and malaria. *Acta Biomaterialia* **1**, 15–30.

TRAN-SON-TAY, R., SUTERA, S. P. & RAO, P. R. (1984) Determination of RBC membrane viscosity from rheoscopic observations of tank-treading motion. *Biophys. J.* **46**, 65–72.

TSUKADA, K., SEKIZUKA, E., OSHIO, C. & MINAMITANI, H. (20010 Direct measurement of erythrocyte deformability in diabetes mellitus with a transparent microchannel capillary model and high-speed video camera system. *Microvasc. Res.* **61**, 231–239.

YOON, Y. Z., KOTAR, J., YOON, G. & CICUTA, P. (2008) The nonlinear mechanical response of the red blood cell. *Phys. Biol.* **5**, 036007.